applied sciences

MDPI

Article

Process Regime Mapping of Green Picosecond Laser Delamination Through Glass in POE Photovoltaic Laminates After Field Aging

Szymon Tofil [1,2,3,4,*], Shuyang Lin [1], Qunli Zhang [1,3], Leonardo Orazi [5,6], António B. Pereira [7], Liang Wang [1,3], Xinran Liu [1] and Jianhua Yao [1,3]

1 Institute of Laser Advanced Manufacturing, Zhejiang University of Technology, No. 288 Liuhe Road, Liuxia Subdistrict, Xihu District, Hangzhou 310023, China
2 Moganshan Institute, Zhejiang University of Technology, Kangqian District, Deqing 313200, China
3 Joint International Research Laboratory on High-End Equipment Laser Manufacturing of Zhejiang Province, No. 288 Liuhe Road, Liuxia Subdistrict, Xihu District, Hangzhou 310023, China
4 Laser Processing Research Center, Faculty of Mechatronics and Mechanical Engineering, Kielce University of Technology, 7 Av. Tysiąclecia P.P., 25-314 Kielce, Poland
5 Department of Sciences and Methods for Engineering, Università Degli Studi di Modena e Reggio Emilia, 42122 Reggio Emilia, Italy
6 EN&TECH, University of Modena and Reggio Emilia, Piazzale Europa 1, 42124 Reggio Emilia, Italy
7 TEMA—Centre for Mechanical Technology and Automation, Department of Mechanical Engineering, University of Aveiro, Campus de Santiago, 3810-193 Aveiro, Portugal
* Correspondence: tofil@tu.kielce.pl

Featured Application

The screening map can guide the selection of laser programs for further studies of interface opening in field-aged POE-rich photovoltaic laminates. Quantitative adhesion, recovery yield, and product quality require separate validation.

Abstract

This study maps operational separation responses in cut fragments from one field-aged crystalline-silicon photovoltaic module containing a polyolefin elastomer (POE)-rich encapsulant. Through-glass irradiation used a 532 nm picosecond laser and eighteen combinations of repetition rate (100–300 kHz), controller setting (50% or 100%), and scan speed (1000–2000 mm s^{-1}). After cooling, one operator assessed corner-initiated manual opening. Responses were classified by sustained opening, interface-opening sequence, and visually estimated released area. Two additional fragments were tested for each of four selected conditions. At 300 kHz and 1000 mm s^{-1}, all three fragments at the 50% setting (G13) showed limited opening with perceived greater resistance, whereas all three at 100% (G16) showed direct release of the glass–POE package from silicon. All three G4 fragments reached full-area separation, with variable or indeterminate interface-opening sequence. A separate specimen processed at 600 kHz fragmented. Local SEM and EDS documented selected exposed silicon-side fields after opening. The resulting map identifies laser programs for gaining access to material interfaces for subsequent recovery studies. Recovery yield and functional product quality were not evaluated.

Keywords: photovoltaic recycling; polyolefin elastomer; POE; laser delamination; picosecond laser; 532 nm; through-glass irradiation; process regime mapping; crystalline silicon

Check for updates

Academic Editor: Evangelos Z. Kordatos

Received: 1 October 2026
Revised: 9 November 2026
Accepted: 11 November 2026
Published: 18 November 2026

Copyright: © 2026 by the authors. Licensee MDPI, Basel, Switzerland. This article is an open access article distributed under the terms and conditions of the Creative Commons Attribution (CC BY) license.

1. Introduction

The continuing deployment of crystalline-silicon (c-Si) photovoltaic (PV) modules is creating a growing end-of-life material stream in which glass, aluminum, polymeric encapsulants, silicon and metallic conductors remain integrated in a durable laminated architecture [1–5]. Bulk comminution, understood here as crushing or grinding the laminate before selective separation of its layers, can mix glass, polymer and cell-derived material in the recovered fractions [3]. Selective laminate opening is therefore important when the objective is access to silicon and metallization rather than production of a mixed crushed fraction.

The encapsulant is the polymeric layer that bonds and protects the cell assembly [6]. Polyolefin encapsulants cover multiple formulations; adhesion and degradation can depend on composition and exposure conditions [7–10]. FTIR-ATR and TGA/DTG measurements on material from the same commercial module supported its identification as POE-rich; local SEM/EDS observations also documented heterogeneous residues [11]. Here, additional fragments from that module were used to study opening responses. The chemical and thermal characterization was not repeated on these fragments.

Laser processing offers spatially selective energy delivery and has consequently been investigated for laminate opening, interface weakening, and recovery of PV materials [12–19]. Li et al. combined near-infrared irradiation with mechanical peeling of EVA from c-Si cells [12]. Bin Anwar et al. compared 355, 532, and 1064 nm nanosecond irradiation for releasing the glass–EVA assembly from silicon at the EVA–Si interface and documented damage to the antireflection layer under the investigated conditions [13]. Sanathi et al. demonstrated multi-interface delamination using femtosecond pulses [14], whereas Aninat et al. used picosecond near-infrared irradiation interacting primarily with silicon to weaken the encapsulant–wafer interface [15]. Zhang et al. applied continuous-wave laser processing to release cells from glass–glass modules [16]. Collectively, these studies show that macroscopically successful release and preservation of a functional cell surface are distinct endpoints.

The measurements used to characterize those endpoints also differ. Bin Anwar et al. reported a beam diameter of 6.7 ± 0.2 mm for the 532 and 1064 nm configurations and used at least five specimens per fluence for their pressure-based detachment tests [13]. Aninat et al. reported local EDS compositions with accompanying $\pm$ values from three 350×510 µm areas per fluence region in Sample D, measured at an accelerating voltage of 7 kV [15]. The present study records categorical opening outcomes and local EDS descriptors under a different protocol.

Earlier work on picosecond processing of elastomers and laser micropatterning of polyethylene shows that polymer surface responses depend on coupled beam and scan parameters [20,21]. A broader review describes the range of physical and chemical responses involved in laser ablation of polymers [22]. This background motivates screening combinations of repetition rate, controller setting, and scan speed in the present POE-rich laminate. It does not identify the mechanism responsible for any particular opening response observed here.

The present study evaluates laboratory-scale opening of manually cut laminate fragments. The procedure records whether opening can be sustained, which interface opens, and whether the glass–POE assembly separates directly from silicon. The research question was how repetition rate, controller setting, and scan speed relate to the operational separation modes of a field-aged c-Si/POE laminate irradiated through glass. The 18-condition matrix was used to locate contrasting opening responses. Targeted repeats at 1000 mm s^{-1} tested whether the contrasts between 50% and 100% settings recurred at 100 and 300 kHz.

A separate higher-frequency condition was examined outside the primary matrix. Local SEM and EDS documented selected post-opening surfaces as a complementary endpoint.

2. Materials and Methods

This section describes the source laminate, optical configuration, screening matrix, program-specific power readings and specimen irradiation intervals, operational response classification, and SEM/EDS procedure. The workflow was designed to preserve traceability from each saved laser program to its macroscopic response and selected local surface characterization.

2.1. Photovoltaic Module and Specimens

The investigated material originated from a commercial c-Si PV module that had operated under field conditions for approximately five years. The module was manufactured by Jinzhou Yangguang Jinmao Photovoltaic Technology Co., Ltd. (Solariga Energy, Jinzhou, China), model JMPV-6DM/72-360, with a nominal maximum power of 360 W under standard test conditions. The module label indicated compliance with IEC 61215 and IEC 61730. Complete service-history and degradation records were unavailable; the material was therefore treated as a field-aged commercial laminate with an incompletely documented service history [11].

The front glass thickness was 3.0 mm. Previous FTIR-ATR, TGA/DTG and SEM/EDS analyses of material from the same module supported the POE-rich assignment of the encapsulant and documented heterogeneous inorganic residues [11]. In this manuscript, POE refers to the encapsulant type previously assigned for this module. Carbon signals on the exposed silicon-side surfaces are reported as local EDS contributions of undetermined origin.

The full-sized module was cut manually into laboratory fragments. Their dimensions were not uniform; approximately 36 × 36 mm describes the specimen size rather than an identical dimension for every fragment. The cut fragments contained pre-existing glass cracks and irregular edges. The present screening therefore concerns manually prepared laminate fragments rather than intact, uniformly dimensioned modules.

The 18 primary screening specimens were designated G1–G18. A separate specimen, S1, was processed under a condition outside the primary matrix. Two additional fragments were processed for each of G1, G4, G13, and G16 and were designated Gx(2) and Gx(3); the original specimen retained the code Gx.

2.2. Laser System and Irradiation Geometry

Irradiation was performed using the green 532 nm output of a PICO-355-30* picosecond laser system (Wuhan Huaray Precision Laser Co., Ltd., Wuhan, China). The manufacturer specifies a pulse duration below 10 ps. The beam was scanned through the front glass toward the encapsulant-cell interface. The optical head used a quartz F-theta scan lens, HY-SL-532-100-160-M85L41 (10CA-FSA-4P-D90), manufactured by Suzhou Huaying Photoelectric Instrument Co., Ltd. (Suzhou, China). The manufacturer's drawing specified an effective focal length of 160 mm, a back working distance of 210 mm, a 100 × 100 mm scan field, a 10 mm entrance-beam diameter, nominal $1/e^2$ spot diameters of 15 µm at the field center and 17 µm at the field edge, and transmission above 99% at 532 nm.

The workstation axial setting was 3.85 mm above the specimen underside, with the POE–Si interface as the nominal target. The scan-lens spot specifications do not determine the waist or local pulse fluence at that interface after transmission through 3 mm of glass. Each program specified one pass of parallel hatch lines over a 45 × 45 mm field with 0.08 mm spacing. The nominal line scan speeds were 1000, 1500, or 2000 mm s^{-1}. The field was deliberately extended beyond the fragment edges to accommodate variations in dimensions

and outline from manual cutting. The nominal hatch geometry specifies the line layout; turn paths, line transitions, and scanner acceleration were not independently characterized. Processing took place in ambient air without a water layer or assist gas.

Figure 1 illustrates the experimental workflow. Panel (a) shows the dimensional measurement of a representative cut laminate fragment. Panel (b) schematically illustrates single-pass raster irradiation through the front glass toward the nominal POE–Si interface. Opening of the primary specimens began after irradiation of the 18-specimen series. The specimens cooled passively under laboratory conditions before corner-initiated manual opening, as illustrated in panel (c). Macroscopic documentation and local SEM/EDS characterization of selected specimens are represented in panel (d). The fixed parameters and equipment are summarized in Table 1.

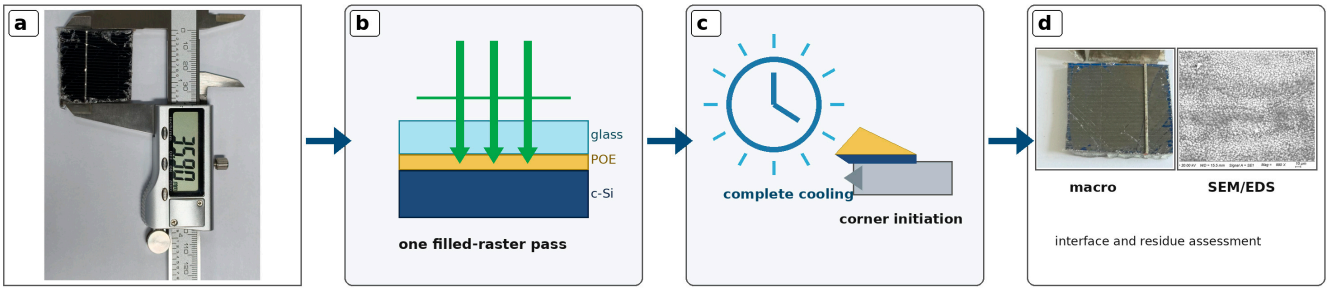


Figure 1. Experimental workflow: (**a**) specimen dimension measurement; (**b**) through-glass raster irradiation; (**c**) cooling and corner-initiated manual separation; and (**d**) macroscopic examination and local SEM/EDS characterization of selected specimens.

Table 1. Material, optical configuration, and fixed experimental parameters.

Item	Specification
PV module	Solariga Energy JMPV-6DM/72-360, 360 W; approximately five years of field service
Encapsulant	POE-rich material previously identified in fragments from the same parent module [11]
Glass thickness	3.0 mm
Specimen size	Approximately 36 × 36 mm, with fragment-to-fragment variation due to manual cutting
Laser source	PICO-355-30 green picosecond output
Wavelength and pulse duration	532 nm; <10 ps according to manufacturer documentation
Scan lens	HY-SL-532-100-160-M85L41 (10CA-FSA-4P-D90); EFL 160 mm; nominal 15–17 µm $1/e^2$ spot
Focal-plane setting	Workstation axial setting: 3.85 mm above the specimen underside; nominal POE–Si target; buried-interface waist not measured
Raster	45 × 45 mm; 0.08 mm hatch; one pass
Main factors	100, 200 and 300 kHz; low 50% and high 100%; 1000, 1500 and 2000 mm s^{-1}
Power measurement	Ophir F150A-BB-26-V1 sensor with Ophir NOVA II meter, Ophir Optronics Solutions Ltd., Jerusalem, Israel
SEM and EDS	ZEISS EVO18 with Bruker Nano XFlash Detector 5010

Pulse duration, nominal spot diameter, and scan-lens transmission are manufacturer specifications; program-specific measured powers are reported in Table 2.

Table 2. Primary screening programs and recorded sensor-plane power and irradiation intervals.

f (kHz)	Code	Setting	v (mm s^{-1})	$P_{scan,\ mean}$ (W)	t_{irr} (s)
100	G1	low 50%	1000	1.0	20.3
	G2	low 50%	1500	0.8	14.9
	G3	low 50%	2000	0.6	10.2
	G4	high 100%	1000	2.7	20.3
	G5	high 100%	1500	1.7	14.9
	G6	high 100%	2000	1.3	10.2
200	G7	low 50%	1000	1.8	20.3
	G8	low 50%	1500	1.3	14.9
	G9	low 50%	2000	1.0	10.2
	G10	high 100%	1000	5.0	20.3
	G11	high 100%	1500	3.6	14.9
	G12	high 100%	2000	2.7	10.2
300	G13	low 50%	1000	3.0	20.3
	G14	low 50%	1500	2.0	14.9
	G15	low 50%	2000	1.6	10.2
	G16	high 100%	1000	7.9	20.3
	G17	high 100%	1500	5.3	14.9
	G18	high 100%	2000	4.0	10.2

$P_{scan,mean}$ is the program-specific mean power reading at the sensor plane. t_{irr} is the mean of three manual timings of the irradiation interval on the specimen for that program (Section 2.4). Operational codes are defined in Table 3; outcomes are reported in Section 3 and Table S1.

Table 3. Operational classification used for the macroscopic separation response.

Code	Operational Criterion
D0	No effective separation. A sustained opening front could not be initiated or propagated using the fixed procedure.
D1	Limited separation. Local opening was initiated, but the visually estimated released area remained below approximately 25% of the observable area.
D2	Effective sequential separation. The glass–POE and POE–Si interfaces were opened in sequence over most of the observable area.
D3	Effective direct release. The glass–POE package was released directly from Si over essentially the full observable area.
DX	Destructive fragmentation. Loss of specimen integrity prevented evaluation as controlled delamination.
R	Greater mechanical resistance was perceived by the operator during corner-initiated manual opening. No force was measured.

The fixed optical arrangement and nominal raster defined the common irradiation geometry for the screening programs described in Section 2.3.

2.3. Screening Matrix and Low-High Convention

The primary series was a complete 3 × 2 × 3 screening matrix comprising three pulse repetition rates, two controller settings, and three scan speeds. Each G code denotes one physical specimen and one unique program. The design was used to locate qualitatively distinct response regimes, not to fit a response surface or claim an optimized operating point.

At each pulse repetition rate, the controller was set to either 50% (low) or 100% (high). These labels describe relative controller commands within a given frequency configuration. They are not two universal absolute optical powers shared across all frequencies and scan speeds. Each program is therefore reported with its own measured mean power, $P_{scan,mean}$.

For example, 7.9 W is the measured value for G16 at 300 kHz, the 100% controller setting and 1000 mm s^{-1}; it is not the catalog maximum of the source.

Table 2 lists the primary programs and measurement records. Operational codes are defined in Table 3; the observed specimen responses are presented in Section 3 and Table S1.

The tested programs combine repetition rate, controller setting, and scan speed. Each program is accompanied by its own power-sensor reading, obtained with the Ophir sensor and NOVA II meter described in Section 2.4. The low and high labels denote controller settings rather than universal absolute optical powers.

2.4. Power Measurement and Timing Records

For each scan program, the average optical power $P_{scan,mean}$ was measured using an Ophir F150A-BB-26-V1 thermopile sensor connected to an Ophir NOVA II meter (Ophir Optronics Solutions Ltd., Jerusalem, Israel). The sensor was positioned downstream of the final F-theta lens and upstream of the nominal focal plane. At that position, the entire scan footprint was contained within the 26 mm sensor aperture. The same sensor position and alignment were used for all programs. The readings describe optical power after the scan optics and before transmission through the specimen glass. The manufacturer specifies a power measurement accuracy of ±3% for this sensor at 532 nm [23].

One operator (S.T.) used a stopwatch to measure the specimen irradiation interval. Timing began when the scanning beam first reached the specimen surface and ended when irradiation of that specimen was complete. The programmed field extended beyond the specimen edges, and the timed interval was shorter than the full program execution time. For each primary program, t_{irr} is the arithmetic mean of three stopwatch timings. The reported means were 20.3, 14.9 and 10.2 s at nominal scan speeds of 1000, 1500 and 2000 mm s^{-1}, respectively. The stopwatch was operated independently of the laser emission signal. Sensor-plane power and the specimen irradiation intervals are reported separately.

2.5. Additional Condition Outside the Primary Matrix

A separate fragment, S1, was processed at 600 kHz with the controller set to 100% and a nominal scan speed of 1000 mm s^{-1}. The program used the same single-pass raster geometry as the primary series. The mean optical power recorded at the sensor plane was 14.7 W, and the manually timed irradiation interval on the specimen was 20.3 s. Because 600 kHz was outside the primary range of 100–300 kHz, S1 was treated as a separate exploratory condition and was not included in the process regime map or the targeted repeat series. The specimen-level record for S1 is provided in Table S2.

2.6. Cooling, Operational Separation Test and Optical Documentation

The 18 primary specimens were irradiated before the opening series began. The specimens cooled passively under laboratory conditions. Cooling times and specimen temperatures were not recorded. The test was designed to assess opening after cooling; opening at elevated temperature was not assessed.

The same operator (S.T.) used the same small flat-blade screwdriver for all opening tests. Each test began at the right-hand corner of the edge first reached by the laser scan, as viewed by the operator. The operator chose the right side because he was right-handed. The operator recorded whether an opening front could be sustained, which interface opened first, whether the glass and POE moved as one package, the approximate released-area category, and whether the specimen lost integrity. Macro photographs documented the specimens before irradiation, after irradiation, and after opening when opening was possible.

This procedure screened whether and how the interfaces opened under each program. It did not use a controlled peel geometry or a force-measurement fixture for the rigid,

cracked specimens [24]. The observed opening sequence and visually estimated released area define the operational classes in Table 3. Resistance felt by the operator is qualitative; no separation force or adhesion energy was measured.

The operational definitions in Table 3 were applied to the primary series and targeted repeats. All primary specimens and S1 received one primary operational code. For the targeted repeats, agreement was assessed at the level of the broad separation endpoint. Where the recorded opening sequence did not distinguish D2 from D3 unambiguously, the unresolved sequence is documented in Table S2 rather than expressed as a combined response class. The optional suffix R denotes greater mechanical resistance perceived by the operator during the opening procedure. It does not change the primary D class. Macro photographs constituted the optical documentation used in the present study; no confocal topography or areal-roughness parameters are reported.

Each classified specimen received one primary D code. The D codes record the observed opening outcome. D1-R, as in G13 and G14, denotes limited opening accompanied by perceived greater mechanical resistance. It is not a different separation class or an estimate of adhesion strength.

2.7. SEM and EDS Characterization

Three primary specimens were selected purposively for SEM: G1 as a low-frequency limited-release condition, G8 as an intermediate sequential-separation condition, and G16 as the direct-release condition. Local EDS was restricted to the contrasting G1 and G16 specimens. This selection, summarized in Table 4, was intended to document characteristic local states and does not imply statistical homogeneity of a complete specimen or of its repeats.

Table 4. Purposeful selection of primary specimens for SEM and EDS.

Specimen	Program	Analysis
G1	100 kHz; 50% controller setting (low); 1000 mm s^{-1}; 1.0 W	SEM and EDS
G8	200 kHz; 50% controller setting (low); 1500 mm s^{-1}; 1.3 W	SEM
G16	300 kHz; 100% controller setting (high); 1000 mm s^{-1}; 7.9 W	SEM and EDS

Specimen selection was purposive and intended to compare contrasting macroscopic responses.

Surface morphology was examined using a ZEISS EVO18 scanning electron microscope (Carl Zeiss AG, Oberkochen, Germany) equipped with a Bruker Nano XFlash Detector 5010 EDS detector (Bruker Nano GmbH, Berlin, Germany). SEM and EDS examined the exposed silicon-side surface after opening. The specimens were attached from the rear side using conductive carbon adhesive and were examined without sputtered carbon or gold coating. SEM images were acquired at 20.0 kV in SE1 mode, with working distances of approximately 15–18 mm and magnifications from 50× to 5000×. EDS maps and spectra were acquired at 20 kV using the specimen preparation described above, with a live time of approximately 10 s per spectrum.

EDS results were evaluated for C, N, O, and Si. Because the 20 kV interaction volume extended substantially into the silicon substrate, the values were treated as local semi-quantitative descriptors. They were not converted into residual-POE thickness, polymer coverage, SiNx thickness, or proof of chemical cleanliness. More surface-sensitive and chemically specific methods would be required for those endpoints.

The selected specimens therefore anchor microscopy to three macroscopically distinct response classes, while the analytical scope remains local and descriptive. No inference about whole-specimen residue coverage or repeat-to-repeat surface variance is made from these fields.

3. Results and Discussion

Results are presented from the destructive S1 condition through the primary matrix, targeted repeats, regime map, and local microscopy. Macroscopic separation behavior is discussed together with surface evidence because these observations represent complementary endpoints of the same screening study.

3.1. Destructive Fragmentation Under the S1 Condition

The mechanically cut S1 specimen showed extensive fragmentation and loss of integrity after irradiation under the separate 600 kHz configuration (Figure 2). This outcome was classified as DX. Figure 2a shows cracks already present before laser treatment. Their contribution to fragmentation was not isolated. Only one S1 specimen was tested, and its frequency and measured power both differed from G16. The observation therefore does not isolate a frequency or power effect and does not determine a general damage threshold. Competing interfacial modification, polymer degradation, and substrate-damage mechanisms are discussed in the broader laser-processing literature [22,25,26].

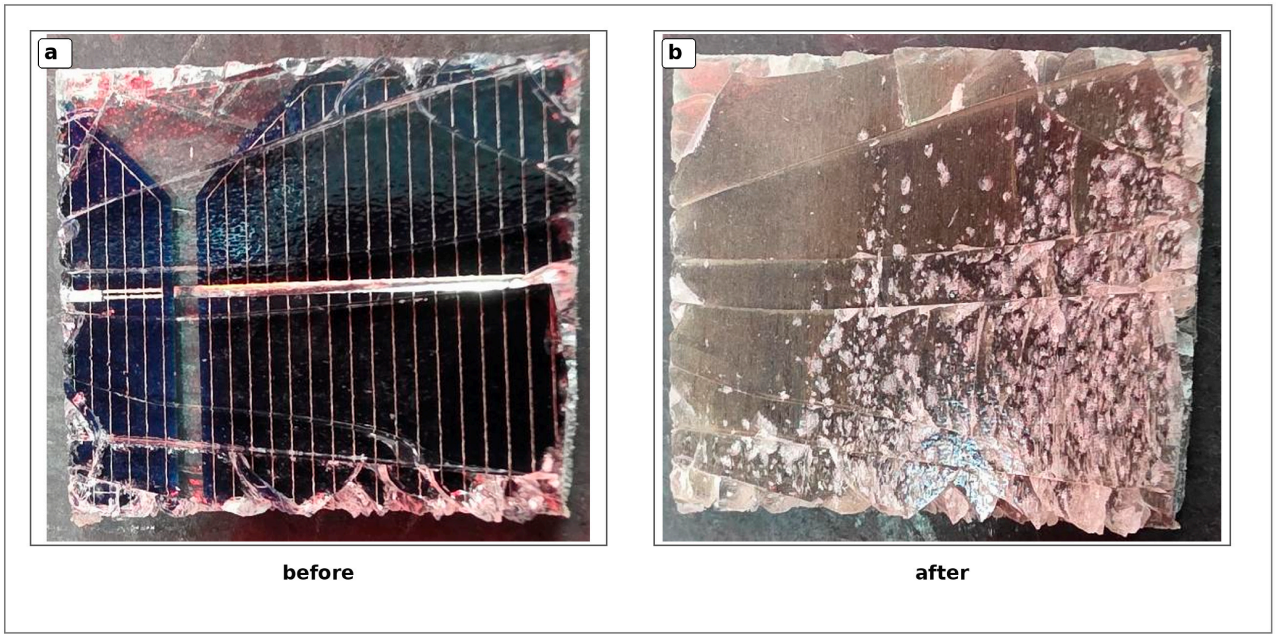


Figure 2. Specimen S1 before (**a**) and after (**b**) irradiation at 600 kHz, the 100% controller setting and 1000 mm s^{-1}, with a reported sensor-plane mean power of 14.7 W.

The S1 observation records a destructive outcome under the tested configuration. It does not locate a general transition boundary or demonstrate that all conditions between G16 and S1 are destructive.

3.2. Macroscopic Response Across the Primary Matrix

The primary screening specimens showed operational classes D0–D3 (Figures 3 and 4; Table S1). At 100 kHz and the 50% controller setting, G1 showed limited local separation (D1), whereas G2 and G3 showed no effective separation (D0). At the 100% controller setting, the primary G4, G5, and G6 specimens showed sequential opening of the glass–POE and POE–Si interfaces (D2). At 200 kHz, all six primary specimens were classified as D2.

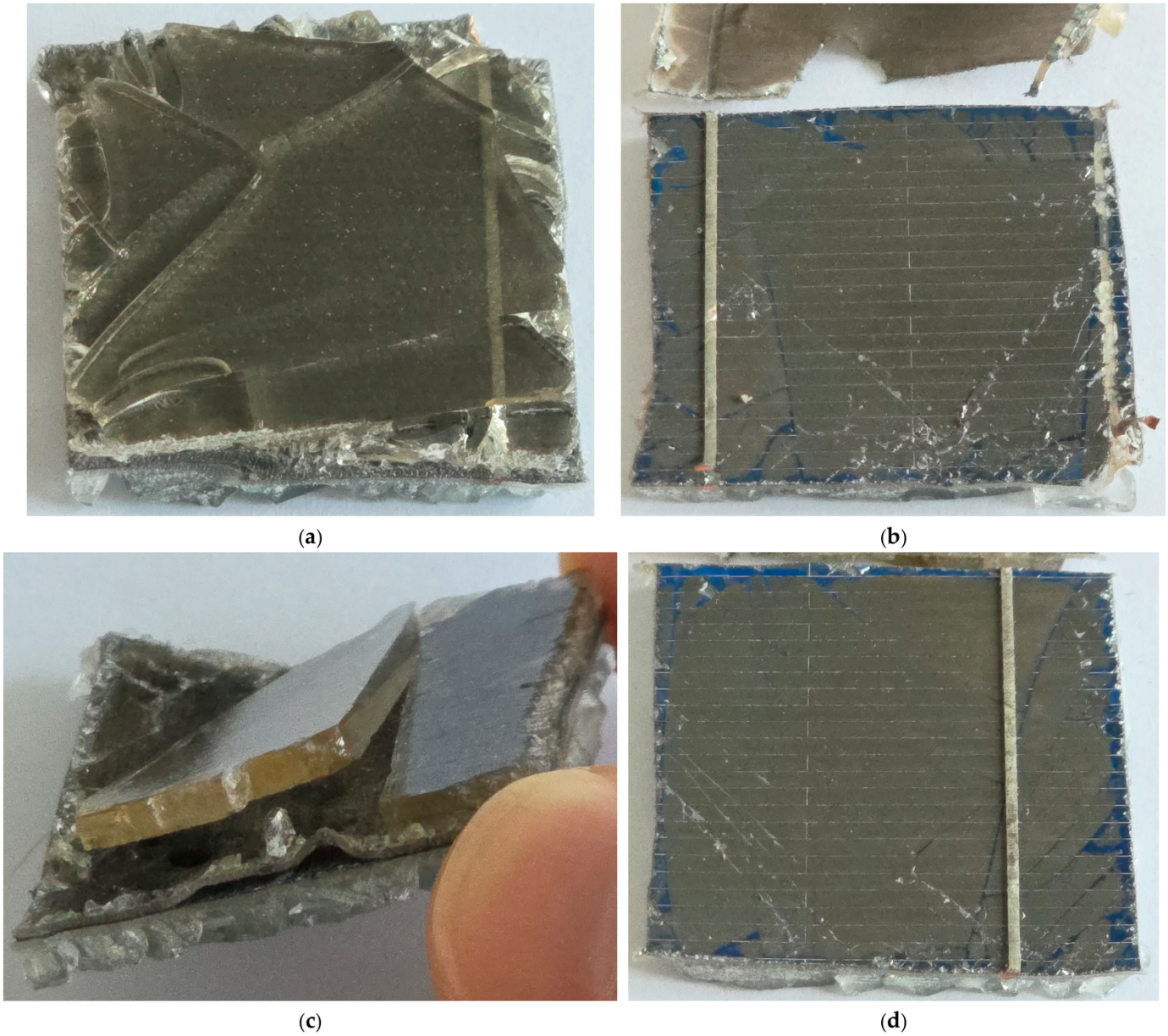


Figure 3. Selected primary-screening responses: (**a**) G2, no effective separation (D0); (**b**) G10, sequential opening (D2); (**c**) G13, limited opening with operator-perceived greater mechanical resistance (D1-R); and (**d**) G16, direct release of the glass–POE package from Si (D3).

At 300 kHz and the 50% controller setting, G13 and G14 were classified as D1-R, whereas G15 was D2. R denotes operator-perceived mechanical resistance during the opening procedure. No temperature history or before–after chemical analysis was obtained to identify the cause of the G13/G14 response.

At 300 kHz with the controller set to 100% (high), G16 exhibited direct release: the glass and POE moved together and separated from silicon over essentially the full observable area, corresponding to D3. G17 and G18 allowed effective sequential separation and were classified as D2. Representative outcomes for G2, G10, G13 and G16 are compared in Figure 3.

Figure 3 illustrates the distinction between ineffective opening, sequential separation, limited opening with apparently increased resistance, and direct package release. The classifications describe the recorded opening procedure; final photographs alone do not reconstruct the complete interface-opening sequence or quantify separation force.

By unaided visual inspection, all primary specimens showed POE darkening, including G10 and G16. The apparent degree of darkening varied among specimens. Darkening was excluded from the opening criteria, and optical transmittance was not measured. Laser-treated POE-rich residues from the same module were characterized in earlier work [11].

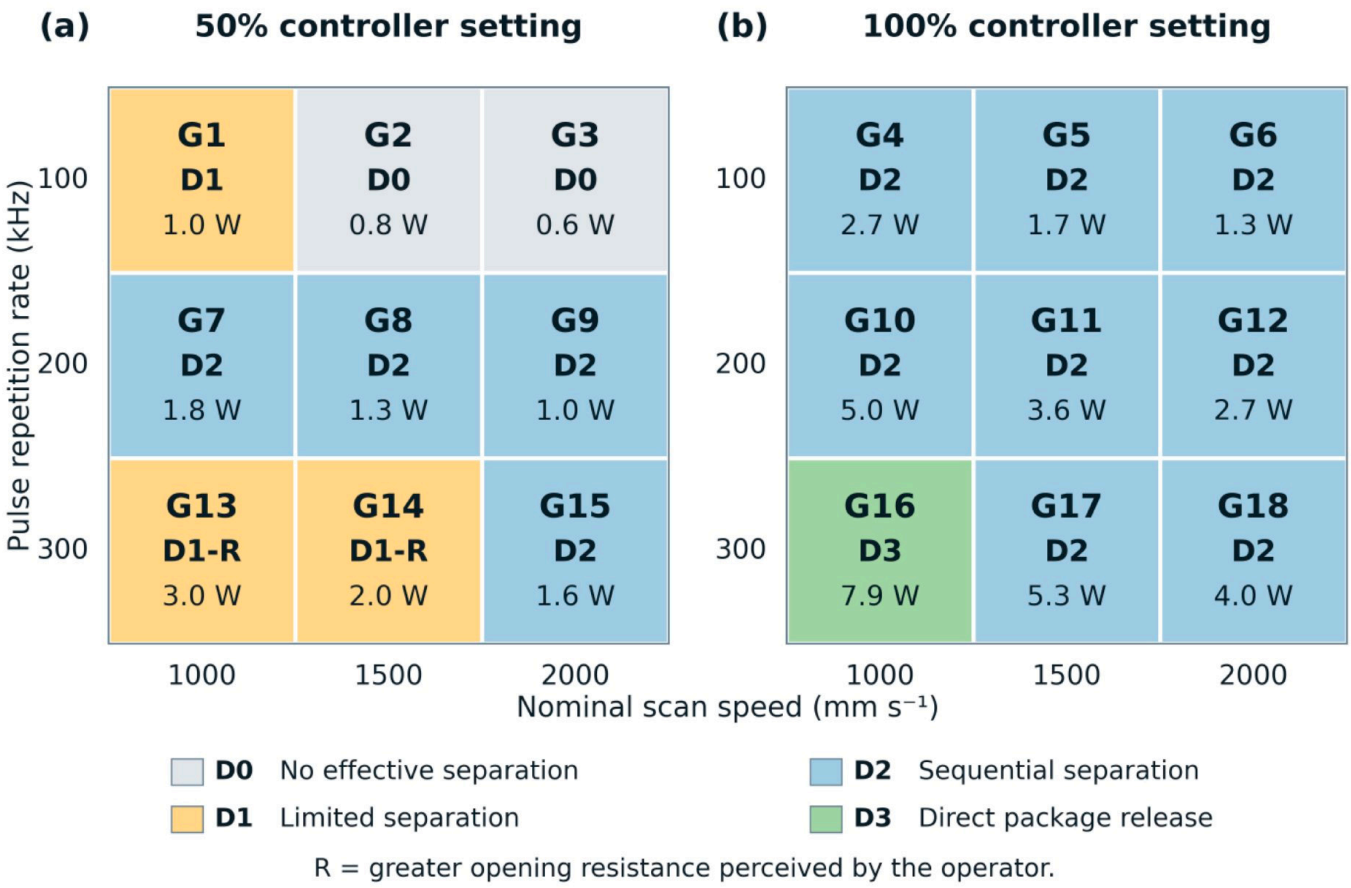


Figure 4. Observed operational response classes for the low 50% (**a**) and high 100% (**b**) controller settings. Cell colors denote the primary D0–D3 classes. The suffix R denotes greater opening resistance as perceived by the operator.

3.3. Targeted Confirmation of Discriminating Conditions

The initial 18-point matrix was deliberately broad, but a single specimen per point cannot establish full-matrix repeatability. Two additional specimens were therefore processed for G1, G4, G13, and G16. These four conditions were selected because they create matched low-high contrasts at 1000 mm s^{-1} for 100 and 300 kHz and span limited opening, sequential opening, and direct package release. Table 5 summarizes the targeted confirmation.

The three tested fragments agreed in the broad separation endpoint for each selected condition. For G1, G13, and G16, the recorded outcomes were D1, D1-R, and D3, respectively; for G4, agreement concerned successful separation despite variation in the opening sequence. These observations support within-study consistency for the selected conditions but do not establish full-matrix repeatability or quantify separation force.

For G4, all three tested fragments reached full-area separation, but the recorded opening sequence differed: the primary G4 specimen was D2, G4(2) was D3, and G4(3) could not be assigned unambiguously to D2 or D3. The repeat series therefore supports consistency of the broad release endpoint for these fragments, while the separation path remained variable or indeterminate. The present observations do not identify the cause of that variation.

Table 5. Targeted confirmation experiments for four discriminating conditions.

Code	Program	n [1]	Broad Operational Result	Broad-Outcome Agreement
G1	100 kHz; 50% controller setting (low); 1000 mm s^{-1}	3	Limited local separation (<25% visually estimated); no effective full-area release.	3/3
G4	100 kHz; 100% controller setting (high); 1000 mm s^{-1}	3	Effective full-area separation in all three fragments; the original G4 was D2, but the opening sequence differed in the repeats.	3/3
G13	300 kHz; 50% controller setting (low); 1000 mm s^{-1}	3	Limited separation (<25% visually estimated) with apparently increased opening resistance.	3/3
G16	300 kHz; 100% controller setting (high); 1000 mm s^{-1}	3	Direct release of the glass–POE package from Si over essentially the full observable area.	3/3

[1] n includes the original specimen and two targeted repeats. Agreement refers to the broad separation endpoint and does not imply identical separation force. For G4, 3/3 denotes successful full-area separation, not agreement in the D2 interface-opening sequence. Repeat specimens used the corresponding saved program; the primary program power values were not independently remeasured for every fragment, as indicated in Table S2.

3.4. Process Regime Map

Figure 4 places the broad operational modes in the frequency-speed plane for the low and high controller settings. Each cell includes the physical specimen code and measured $P_{scan,mean}$. The figure is a categorical map of observed specimens, not an interpolation, probability surface, or statistical optimization.

At the 50% setting, all three tested speeds gave D2 at 200 kHz. At 300 kHz, the 50% setting gave D1-R at 1000 and 1500 mm s^{-1} and D2 at 2000 mm s^{-1}. At 300 kHz and 1000 mm s^{-1}, all three G13 fragments (50%) showed D1-R, and all three G16 fragments (100%) showed D3. At the 50% setting and 1000 mm s^{-1}, the primary responses were limited at 100 kHz, sequential at 200 kHz, and limited again at 300 kHz. The map captures these observed contrasts without assigning an interfacial mechanism or an adhesion threshold. DX occurred only in the separate S1 specimen.

3.5. SEM Morphology of Representative Surfaces

The selected SEM fields on the exposed silicon-side surfaces of G1, G8, and G16 show similar fine textures with local discontinuities and discrete particle-like features (Figure 5). A scratch-like feature and a larger particle are visible in Figure 5c. The selected fields do not support a systematic difference in residue coverage across these conditions. SEM morphology alone cannot establish the identity of the features, the presence of a continuous POE film, or the condition of the antireflection coating. Some discontinuities may originate from specimen preparation or manual opening. Related laser-assisted PV studies show that effective layer release can involve modification or removal of the antireflection coating [13,15,16]. In the present study, the SEM observations do not establish preservation of that coating or retained electrical functionality.

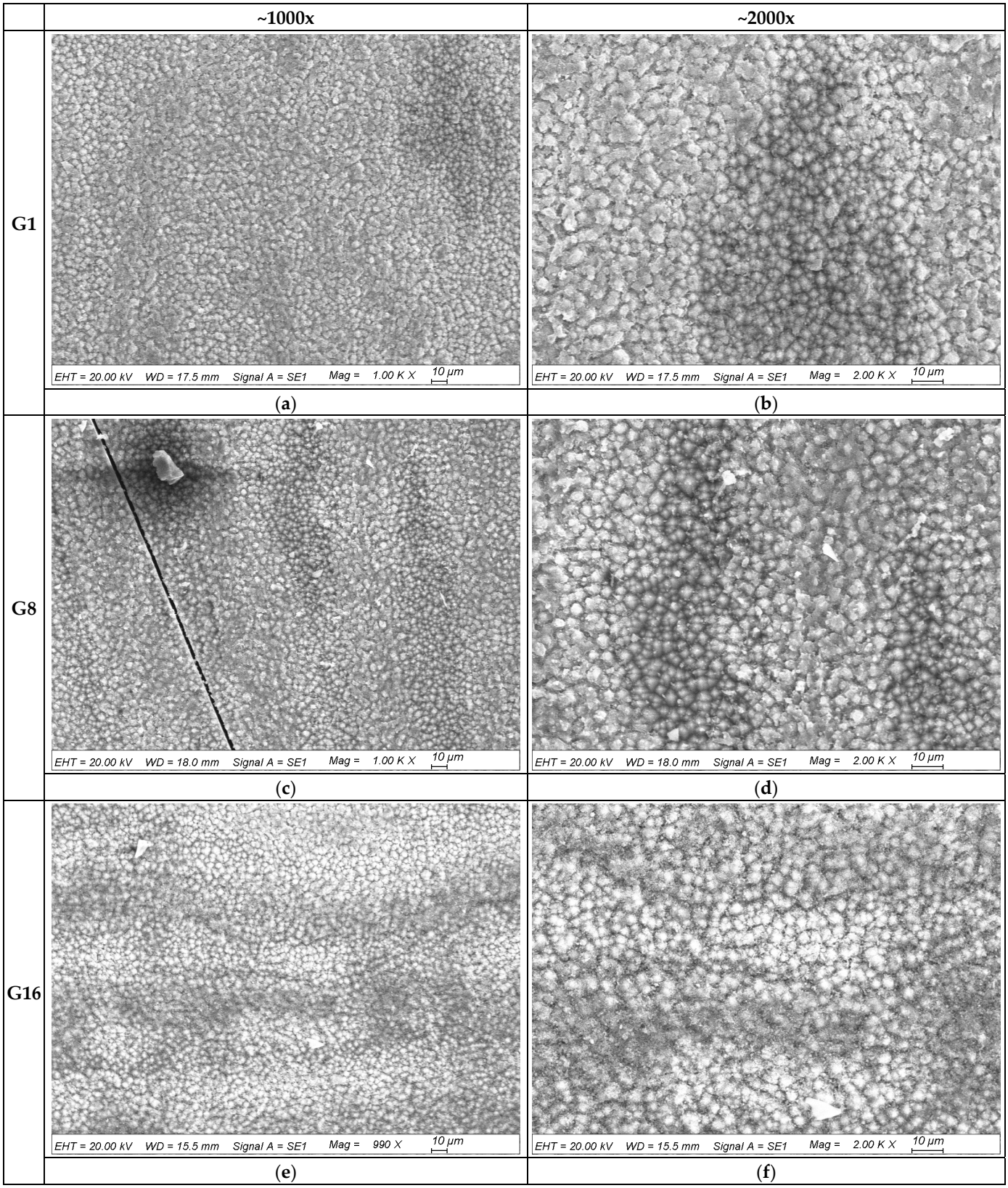


Figure 5. Selected local SEM fields on the exposed silicon-side surfaces of G1 (**a**,**b**), G8 (**c**,**d**) and G16 (**e**,**f**), at approximately 1000× (**a**,**c**,**e**) and 2000× (**b**,**d**,**f**). The fields are not spatially matched between specimens. Scale bars are shown in the source images.

SEM was performed on one primary specimen for each of G1, G8, and G16. No SEM was acquired for the additional repeat fragments. The selected images therefore provide local morphological observations, not a replicated comparison of whole-surface residue coverage.

The SEM comparison therefore supports a distinction between macroscopic opening and local surface state. Direct D3 release in G16 did not establish uniform residue removal or preservation of the cell surface.

3.6. Local Semi-Quantitative EDS Comparison

Table 6 reports local semi-quantitative EDS results for selected G1 and G16 regions. In Figure 6, panels (a–e) show G1 region 2 and panels (f–j) show G16 region 1, as listed in Table 6. Within each group, the SEM image and elemental maps correspond to the same field. The G1 and G16 fields are different selected locations on different specimens. Silicon dominated the analyzed regions, while carbon, nitrogen, and oxygen were also detected. These observations do not establish the origin of the carbon signal or the continuity of the antireflection coating.

Table 6. Local semi-quantitative EDS composition of selected G1 and G16 regions at 20 kV.

Region	C Norm. wt.%	N Norm. wt.%	O Norm. wt.%	Si Norm. wt.%
G1 region 1	21.54	6.53	0.92	71.01
G1 region 2 (Figure 6a–e)	18.61	3.12	1.13	77.14
G16 region 1 (Figure 6f–j)	21.66	4.25	2.66	71.43
G16 region 2	22.33	4.04	2.71	70.93
G16 region 3	20.87	4.32	2.64	72.18

Values are local semi-quantitative normalized EDS results acquired at 20 kV; they do not quantify POE thickness, areal coverage, or chemical cleanliness.

The normalized carbon contribution ranged from 18.61 to 21.54 wt.% in the two selected G1 regions and from 20.87 to 22.33 wt.% in the three selected G16 regions. The ranges overlap, and these spatially unmatched local analyses do not demonstrate a reduction in carbon-containing contributions for G16 relative to G1. Direct release therefore did not establish a carbon-free surface at the analyzed sites.

The oxygen contribution was higher in the selected G16 regions than in G1, but the spatially unmatched regions, purposive field selection, and large 20 kV interaction volume preclude assignment of that difference to laser-induced oxidation. The nitrogen signal may include contributions associated with SiNx or local residue, but EDS at 20 kV cannot establish the continuity or thickness of a nanometer-scale antireflection layer. The EDS spectra were dominated by silicon and showed local carbon contributions; the origin and chemical identity of the carbon signal were not established. Previous characterization of material recovered from the same parent module also revealed heterogeneous carbon-, silicon-, and oxygen-containing contributions [11].

Surface-specific chemical identification would require XPS, Raman spectroscopy, or a suitably designed FTIR-ATR measurement. Those methods are appropriate for mechanistic follow-up, whereas the present EDS data serve as a caution against equating macroscopic delamination with chemical cleanliness.

The elemental maps are interpreted qualitatively. The maps cannot quantify residue coverage or identify the molecular origin of the carbon signal.

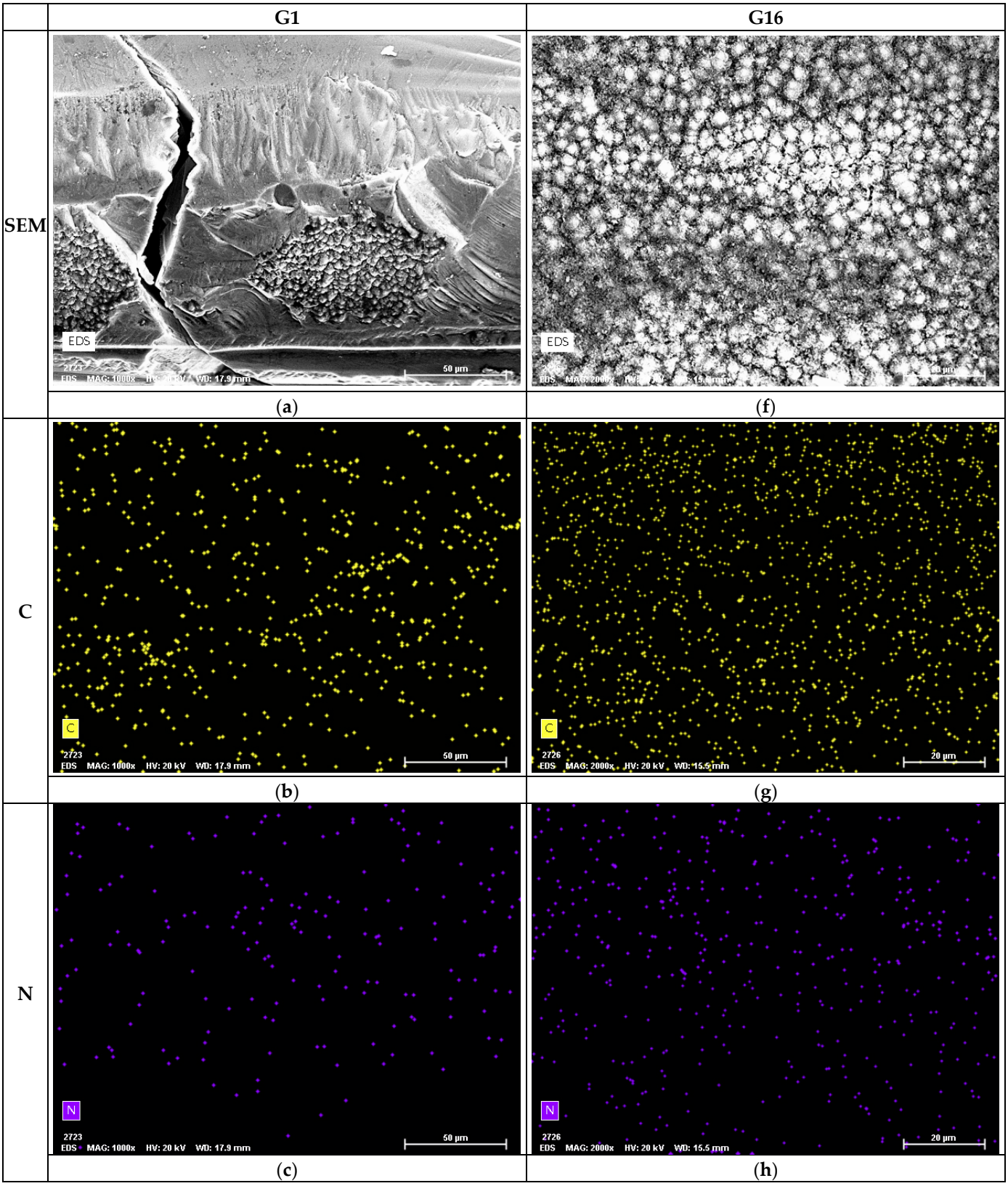


Figure 6. *Cont.*

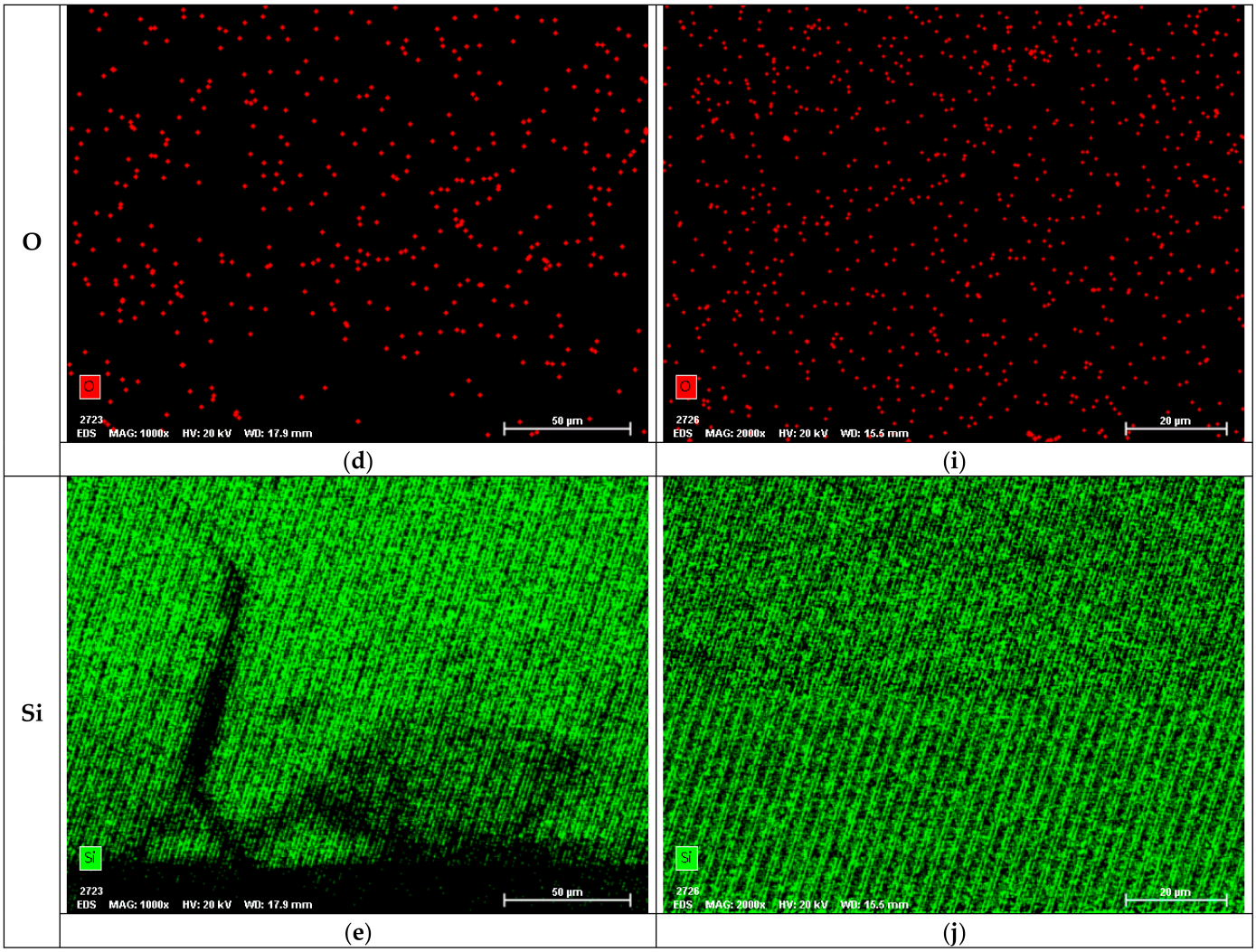


Figure 6. SEM images and qualitative elemental maps from G1 region 2 (**a**–**e**) and G16 region 1 (**f**–**j**), as listed in Table 6. Within each group, the SEM image and the maps show the same field. SEM: (**a**,**f**); C: (**b**,**g**); N: (**c**,**h**); O: (**d**,**i**); Si: (**e**,**j**). Scale bars are shown in the source panels.

3.7. Implications for Downstream Material Recovery

Table 7 compares the endpoints of laser-assisted separation, mechanical and thermal recovery, and process-level recycling assessment. The present study maps opening modes after cooling for a field-aged POE-rich laminate; direct release in G16 reoccurred in three fragments of that module. This result provides a program for further investigation of material recovery. Fiandra et al. assessed recovered fractions and residual carbon after thermal removal of EVA [27]. Zubas et al. evaluated recycling scenarios for a POE glass–glass module and showed that the modeled outcomes depend on the efficiency and substitution assumptions for downstream fractions [28]. The endpoints in Table 7 differ in material, procedure, and scale, so they do not establish a ranking of the routes.

The result should not be extended to functional-cell reuse. The specimens were mechanically cut fragments with pre-existing glass and cell damage, and no electroluminescence, photoluminescence, or current-voltage measurements were performed. The endpoint evaluated here is access to material interfaces for downstream recovery, not preservation of an operational photovoltaic device. Any claim regarding SiN_x integrity, junction quality, or retained electrical performance would require a different specimen format and dedicated electrical validation.

Table 7. Comparison of separation routes, assessment methods and reported endpoints.

Study	Separation or Assessment Route	Reported Endpoint and Basis for Comparison
Li et al. 2022 [12]	1064 nm pulsed irradiation and mechanical peeling of rear EVA after backsheet removal.	Rear EVA removal and assessment of recovered cell material. The rear access route and EVA encapsulant differ from the through-glass POE-rich configuration.
Bin Anwar et al. 2024 [13]	355, 532 and 1064 nm nanosecond irradiation for glass–EVA release from silicon.	Detachment pressure on model specimens, with at least five specimens per fluence, and opening tests on commercial fragments. This pressure endpoint differs from manual opening classes.
Aninat et al. 2026 [15]	Picosecond near-infrared irradiation with thermomechanical separation.	Interface weakening and assessment of SiN_x removal. EDS was used on three regions per fluence at 7 kV. Surface results are not directly comparable to the selected 20 kV fields here.
Kanaujia et al. 2027 [29]	1064 nm nanosecond interface-selective delamination followed by solvent cleaning.	Recovery and assessment of glass and wafers, including glass transmittance after cleaning. The endpoint includes downstream product assessment.
Fiandra et al. 2019 [27]	Mechanical backsheet removal followed by oxidative thermal removal of EVA.	Separation of material fractions and assessment of residual carbon. The elemental-analysis table reports the mean of three analyses and absolute deviation.
Zubas et al. (2027) [28]	Gate-to-gate life cycle and operational-margin assessment of three recycling scenarios for a frameless POE glass–glass module.	Modeled environmental and economic outcomes of downstream recovery. Results depend on assumed fraction recovery and material substitution; this is not a laser separation trial.
Present study	532 nm picosecond irradiation through glass, then manual opening of fragments from one field-aged POE-rich module.	Observed opening modes in 18 programs; four targeted repeat series. G16 direct release in three fragments. Local SEM/EDS, without quantified recovery yield or functional product quality.

3.8. Limitations

- The initial 18-condition matrix used one fragment per condition. Additional repeats were limited to G1, G4, G13 and G16, using material from the same parent module.
- Opening was assessed manually by one operator. Interface-opening sequence and approximate released area were recorded, but force, adhesion energy, and inter-operator agreement were not measured. The effect of the starting corner was not assessed separately.
- The fragments had different dimensions and pre-existing glass damage from manual cutting. A fixed raster larger than the fragments provided a common programmed field, but it did not eliminate specimen-to-specimen variation. The contributions of preparation damage and manual initiation were not isolated by the present comparisons.
- Transferability across modules, manufacturers, encapsulant formulations, and aging histories remains untested.
- The manual timings were independent of the laser emission signal and could not resolve individual laser-on intervals within the scan. Measurement uncertainty was not determined for the complete power measurement in the scanning configuration

or for the manual timings. Pulse energy and beam waist at the buried interface were not measured.

- SEM and EDS examined selected local fields in primary specimens and did not quantify whole-surface coverage or repeat-to-repeat surface variation.
- No in situ temperature history, processed-material DSC, XPS, Raman, or electrical I-V, EL, or PL analysis was obtained. The study does not establish an interfacial mechanism, SiNx integrity, functional-cell reuse, recovery yield, or process-level performance.

4. Conclusions

1. The 18 tested programs mapped distinct opening modes for fragments from one field-aged POE-rich module under 532 nm picosecond irradiation through glass. For example, at the 50% setting and 1000 mm s^{-1}, opening was sequential at 200 kHz and limited at 300 kHz.
2. G16 at 300 kHz, the 100% controller setting and 1000 mm s^{-1} produced direct glass–POE package release from silicon in the primary specimen and two additional fragments.
3. G13 at 300 kHz, the 50% controller setting and 1000 mm s^{-1} remained D1-R in three tested fragments. G4 reached full-area separation in three fragments, but its opening sequence varied or was indeterminate.
4. The separate S1 specimen showed destructive fragmentation under the tested 600 kHz configuration. This single observation does not define a general damage boundary.
5. Local SEM and EDS observations documented heterogeneous post-opening surface states. They did not demonstrate uniform residue removal, SiNx preservation, or retained electrical functionality.
6. The map identifies tested programs for accessing material interfaces before downstream recovery. Quantitative adhesion, recovery yield, throughput, energy demand, and functional product quality were not established.

Supplementary Materials: The following supporting information can be downloaded at: https://www.mdpi.com/article/10.3390/app162211432/s1. The Supplementary Materials contain a photographic overview of the primary specimens G1–G18 (Figure S1), the available photographic records for specimen S1 and the targeted repeat specimens (Figure S2), and specimen-level records for the primary screening series (Table S1) and for specimen S1 and the targeted repeat specimens (Table S2).

Author Contributions: Conceptualization, S.T.; methodology, S.T. and S.L.; investigation, S.T. and S.L.; formal analysis, S.T. and S.L.; data curation, S.T., S.L. and X.L.; resources, Q.Z., L.W. and J.Y.; supervision, Q.Z., J.Y., L.O. and A.B.P.; visualization, S.T., S.L. and X.L.; writing—original draft preparation, S.T.; writing—review and editing, all authors; project administration, S.T. and Q.Z.; funding acquisition, S.T. and A.B.P. All authors have read and agreed to the published version of the manuscript.

Funding: This research was funded by the National Natural Science Foundation of China (NSFC), grant number W2533158. The present study was developed within the scope of the Project Agenda ILLIANCE [C644919832-00000035 | Project no. 46], financed by PRR—Plano de Recuperação e Resiliência under the Next Generation EU from the European Union.

Institutional Review Board Statement: Not applicable.

Informed Consent Statement: Not applicable.

Data Availability Statement: The data presented in this study, including macro photographs, program settings, power and runtime records, and SEM/EDS outputs, are available from the corresponding author on reasonable request. Representative supporting images and the specimen-level response table are provided in the Supplementary Materials.

Acknowledgments: The authors acknowledge the technical and laboratory support provided by the Institute of Laser Advanced Manufacturing, Zhejiang University of Technology, during sample preparation and materials characterization. During the preparation of this manuscript, the authors used ChatGPT (web interface; OpenAI, San Francisco, CA, USA; https://chatgpt.com/, accessed on 9 November 2026) to support language editing, structural organization, and consistency checking. The authors reviewed and edited all AI-assisted outputs and take full responsibility for the content of this publication.

Conflicts of Interest: S.T. serves as a Guest Editor of the Special Issue to which this manuscript is submitted. The authors declare no conflicts of interest.

Abbreviations

The following abbreviations are used in this manuscript:

c-Si	crystalline silicon
DSC	differential scanning calorimetry
EDS	energy-dispersive X-ray spectroscopy
EL	electroluminescence
EVA	ethylene-vinyl acetate
FTIR-ATR	Fourier-transform infrared spectroscopy with attenuated total reflectance
I-V	current-voltage
PL	photoluminescence
POE	polyolefin elastomer
PV	photovoltaic
SEM	scanning electron microscopy
SiNx	silicon nitride
TGA/DTG	thermogravimetric analysis/derivative thermogravimetry
XPS	X-ray photoelectron spectroscopy

References

1. Weckend, S.; Wade, A.; Heath, G. *End of Life Management: Solar Photovoltaic Panels*; International Renewable Energy Agency (IRENA): Abu Dhabi, United Arab Emirates; International Energy Agency Photovoltaic Power Systems Programme (IEA-PVPS): Redfern, Australia, 2016.
2. Farrell, C.C.; Osman, A.I.; Doherty, R.; Saad, M.; Zhang, X.; Murphy, A.; Harrison, J.; Vennard, A.S.M.; Kumaravel, V.; Al-Muhtaseb, A.H.; et al. Technical Challenges and Opportunities in Realising a Circular Economy for Waste Photovoltaic Modules. *Renew. Sustain. Energy Rev.* **2020**, *128*, 109911. [CrossRef]
3. Deng, R.; Zhuo, Y.; Shen, Y. Recent Progress in Silicon Photovoltaic Module Recycling Processes. *Resour. Conserv. Recycl.* **2022**, *187*, 106612. [CrossRef]
4. Cui, H.; Heath, G.; Remo, T.; Ravikumar, D.; Silverman, T.; Deceglie, M.; Kempe, M.; Engel-Cox, J. Technoeconomic Analysis of High-Value, Crystalline Silicon Photovoltaic Module Recycling Processes. *Sol. Energy Mater. Sol. Cells* **2022**, *238*, 111592. [CrossRef]
5. Ngagoum Ndalloka, Z.; Vijayakumar Nair, H.; Alpert, S.; Schmid, C. Solar Photovoltaic Recycling Strategies. *Sol. Energy* **2024**, *270*, 112379. [CrossRef]
6. Lust, S.; Weber, T.; Kuntamukkula, S.R.; Mordvinkin, A.; Wendt, M. Update of Quality Control Tests for New PV Encapsulation Materials. *EPJ Photovolt.* **2024**, *15*, 5. [CrossRef] [PubMed]
7. Oreski, G.; Omazic, A.; Eder, G.C.; Voronko, Y.; Neumaier, L.; Mühleisen, W.; Hirschl, C.; Ujvari, G.; Ebner, R.; Edler, M. Properties and Degradation Behaviour of Polyolefin Encapsulants for Photovoltaic Modules. *Prog. Photovolt. Res. Appl.* **2020**, *28*, 1277–1288. [CrossRef]
8. Oreski, G.; Barretta, C.; Christöfl, P.; Gebhardt, P.; Weiß, K.-A.; Miller, D.C.; Uličná, S.; Kempe, M.; Bruckman, L.S.; Virtuani, A.; et al. What Is a Polyolefin? A Critical Overview of Ethylene Copolymers Used as Solar Photovoltaic Module Encapsulants. *Prog. Photovolt. Res. Appl.* **2026**, *34*, 367–395. [CrossRef]
9. Uličná, S.; Sinha, A.; Miller, D.C.; Habersberger, B.M.; Schelhas, L.T.; Owen-Bellini, M. PV Encapsulant Formulations and Stress Test Conditions Influence Dominant Degradation Mechanisms. *Sol. Energy Mater. Sol. Cells* **2023**, *255*, 112319. [CrossRef]
10. Park, J.H.; Hwang, S.-H. Construction and Characterization of Polyolefin Elastomer Blends with Chemically Modified Hydrocarbon Resin as a Photovoltaic Module Encapsulant. *Polymers* **2022**, *14*, 4620. [CrossRef] [PubMed]

11. Tofil, S.; Lin, S.; Yao, J.; Zhang, Q.; Wang, L.; Orazi, L.; Pereira, A.B.; Oliveira, F.J. Structural and Thermal Assessment of POE Encapsulant Residues from Laser-Treated Photovoltaic Laminate Fragments. *Polymers* **2026**, *18*, 1785. [CrossRef] [PubMed]
12. Li, X.; Liu, H.; You, J.; Diao, H.; Zhao, L.; Wang, W. Back EVA Recycling from C-Si Photovoltaic Module without Damaging Solar Cell via Laser Irradiation Followed by Mechanical Peeling. *Waste Manag.* **2022**, *137*, 312–318. [CrossRef] [PubMed]
13. Bin Anwar, T.; Hanson, K.M.; Lam, K.; Bardeen, C.J. Using Nanosecond Laser Pulses to Debond the Glass-EVA Layer from Silicon Photovoltaic Modules. *Waste Manag.* **2024**, *187*, 275–284. [CrossRef] [PubMed]
14. Sanathi, R.; Bhowmik, S.; Banerjee, S. Femtosecond Laser Assisted, Non-Toxic and Complete Delamination of Photovoltaic Module Layers. *J. Environ. Manag.* **2026**, *402*, 129133. [CrossRef] [PubMed]
15. Aninat, R.; van der Vleuten, M.; Scraigne, J.; Fledderus, H.; Biezemans, A.; Bosman, J.; Gomes, J.; Kuypers, A.; Theelen, M. Laser-Assisted Delamination for High-Value Recycling of Solar Panels. *Prog. Photovolt. Res. Appl.* **2026**, *34*, 297–309. [CrossRef]
16. Zhang, C.; Zhao, Z.; Wang, R.; Zhao, Y.; Wang, X. Separate Silicon Cells from End-of-Life Bifacial Glass Photovoltaic Modules Using Continuous Lasers. *Sci. Rep.* **2026**, *16*, 4986. [CrossRef] [PubMed]
17. Alsulami, B.; Cameron, J.; Feeney, A.; Kettle, J. Laser-Induced Delamination in Aged Silicon Photovoltaic Modules. In Proceedings of the 2025 IEEE 53rd Photovoltaic Specialists Conference (PVSC), Montreal, QC, Canada, 8–13 June 2025; p. 1618.
18. Chowdhury, H.; Chang, N.L.; Song, S.; Xie, Z.; Zuo, J.; Shen, Y. Life Cycle Assessment and Techno-Economic Analysis of a Laser-Based End-of-Life Solar Panel Recycling Process. *Sol. Energy Mater. Sol. Cells* **2026**, *302*, 114358. [CrossRef]
19. Khetri, M.; Gupta, M.C. Recycling of Silver from Silicon Solar Cells by Laser Debonding. *Sol. Energy* **2024**, *270*, 112381. [CrossRef]
20. Antoszewski, B.; Tofil, S.; Mulczyk, K. The Efficiency of UV Picosecond Laser Processing in the Shaping of Surface Structures on Elastomers. *Polymers* **2020**, *12*, 2041. [CrossRef] [PubMed]
21. Tofil, S.; Kurp, P.; Manikandan, M. Surface Laser Micropatterning of Polyethylene (PE) to Increase the Shearing Strength of Adhesive Joints. *Lubricants* **2023**, *11*, 368. [CrossRef]
22. Ravi-Kumar, S.; Lies, B.; Zhang, X.; Lyu, H.; Qin, H. Laser Ablation of Polymers: A Review. *Polym. Int.* **2019**, *68*, 1391–1401. [CrossRef]
23. MKS Ophir Medium–High Power Fan Cooled Thermal Sensors 2026. Available online: https://www.ophiropt.com/mam/celum/celum_assets/op/resources/F50A-BB-18_F100A-PF-DIF-33_F150A-BB-26.pdf (accessed on 9 November 2026).
24. Meena, R.; Pareek, A.; Gupta, R. A Comprehensive Review on Interfacial Delamination in Photovoltaic Modules. *Renew. Sustain. Energy Rev.* **2024**, *189*, 113944. [CrossRef]
25. Zhou, Z.; Sun, W.; Wu, J.; Chen, H.; Zhang, F.; Wang, S. The Fundamental Mechanisms of Laser Cleaning Technology and Its Typical Applications in Industry. *Processes* **2023**, *11*, 1445. [CrossRef]
26. Bernabeu, A.P.; Puerto, D.; Ramirez, M.G.; Nájar, G.; Francés, J.; Gallego, S.; Márquez, A.; Pascual, I.; Beléndez, A. Controlled Photothermal Ablative Processing of Commercial Polymers Minimizing Undesired Thermal Effects under High Frequency Femtosecond Laser Irradiation. *Opt. Laser Technol.* **2024**, *177*, 111069. [CrossRef]
27. Fiandra, V.; Sannino, L.; Andreozzi, C.; Corcelli, F.; Graditi, G. Silicon Photovoltaic Modules at End-of-Life: Removal of Polymeric Layers and Separation of Materials. *Waste Manag.* **2019**, *87*, 97–107. [CrossRef] [PubMed]
28. Zubas, A.R.; Kruopienė, J.; Denafas, G.; La Marca, F.; Bonoli, A. Life Cycle Impact and Economic Assessment of Recycling Strategies for Frameless POE Encapsulated Glass–Glass Photovoltaic Modules. *Sol. Energy Mater. Sol. Cells* **2027**, *310*, 114797. [CrossRef]
29. Kanaujia, P.K.; Owen-Bellini, M.; Mirletz, H.; Young, D.L.; Gupta, M.C. High-Power Laser Recycling of Crystalline Silicon Photovoltaic Modules. *Sol. Energy Mater. Sol. Cells* **2027**, *309*, 114714. [CrossRef]

Disclaimer/Publisher's Note: The statements, opinions and data contained in all publications are solely those of the individual author(s) and contributor(s) and not of MDPI and/or the editor(s). MDPI and/or the editor(s) disclaim responsibility for any injury to people or property resulting from any ideas, methods, instructions or products referred to in the content.